Chemical Engineering Journal 497 (2024) 154560

Contents lists available at ScienceDirect

Chemical Engineering Journal

journal homepage: www.elsevier.com/locate/cej

Porous potassium carbonate granules with enhanced diffusion kinetics for thermochemical heat storage

Delaram Salehzadeh [a], Behrooz Elahi [a], Johan E. ten Elshof [b], Gerrit Brem [a], Mohammad Mehrali [a,*]

[a] Faculty of Engineering Technology, Department of Thermal and Fluid engineering (TFE), University of Twente, 7500 AE Enschede, The Netherlands
[b] University of Twente, MESA+ Institute for Nanotechnology, P.O. Box 217, 7500 AE, Enschede, The Netherlands

ARTICLE INFO

Keywords:
Thermochemical heat storage
Salt hydrates
Potassium carbonate (K_2CO_3)
Porous granules
Hydration kinetics

ABSTRACT

The caking phenomenon poses a significant challenge in thermochemical heat storage systems, which arises from the agglomeration of powdered salt hydrates. This impedes the flow of gas molecules through the reactor bed and negatively impacts the reactions kinetics, leading to decreased overall efficiency of heat storage. To tackle this challenge, an innovative approach is proposed, involving the synthesis of porous potassium carbonate (K_2CO_3) granules using potassium bicarbonate ($KHCO_3$) as a pore former in varying ratios of 10, 20, 40, and 50 wt%. It is essential to note that the maximum amount of $KHCO_3$ for effective granulation is around 50 wt% of the total batch, as exceeding this limit prevents granule formation. This method results in the formation of porous K_2CO_3 granules that are 100% pure and free from any additives that could impact the energy density. In terms of diffusion kinetics, the granules with 40 wt% (K40) and 50 wt% (K50) of $KHCO_3$ demonstrated significant improvements in effective diffusion coefficients in comparison with the K_2CO_3 granule without pore former. Regarding cyclic performance, K_2CO_3 granule without pore former showed slow kinetics and incomplete hydration even after 10 cycles. In contrast, the K40 and K50 granules demonstrated significantly faster hydration kinetics, with K40 achieving complete hydration by the 4th cycle and K50 reaching the highest water loading capacity of 1.5 $mol_{H_2O}/mol_{K_2CO_3}$ from the first cycle. The K50 granule, with a hydrated state density of 1.74 g/cm^3, achieved a volumetric energy density of 0.96 GJ/m^3. Compared to other developed granules, K50 exhibited superior hydration kinetics, positioning it as a promising candidate for thermochemical heat storage applications. This study highlights the potential of modifying pore structure to improve the efficiency of thermochemical heat storage and demonstrates that the wet granulation technique can be effectively utilized for the mass production of salt hydrate granules.

1. Introduction

Thermal energy constitutes a significant proportion of the total energy consumption within a country. The residential sector accounts for 21% of the total energy consumption. Approximately 80% of the aforementioned energy is utilized as thermal energy for the purpose of space heating and the supply of hot tap water [1]. Hence, addressing the thermal energy demand through domestic heat storage could potentially make a substantial contribution to the energy transition [2,3]. Since the direct application of renewable energy sources, like solar or wind power, depends on time and place, a loss-free heat storage technique called thermochemical energy storage (TCES) can be employed [4]. Thermochemical energy storage is based on the reversible chemical reactions that occurs between sorbates and sorbents. The process primarily comprises three phases: charging phase, where thermochemical materials absorb heat and decompose into two substances; storage phase, where the two substances are stored separately; and discharging phase, where the two substances react under specific conditions to release the stored heat [5]. Salt hydrates are a promising category of thermochemical storage materials (TCMs) due to their advantageous characteristics, including a high energy density, operating temperatures compatible with built environments, and the possibility to use water vapor as a sorbate, ensuring safety and environmental friendliness [6].

A comprehensive study by Mazur et al. [1] evaluated 454 salt hydrates and 1073 hydration reactions suitable for household heat storage. Evaluation criteria included scarcity, toxicity, chemical stability, energy density higher than 1 GJ/m^3, suitability for space heating (required temperatures higher than 30 °C) and hot water generation (required temperatures higher than 55 °C), and compatibility with

* Corresponding author.
E-mail address: m.mehrali@utwente.nl (M. Mehrali).

https://doi.org/10.1016/j.cej.2024.154560
Received 29 April 2024; Received in revised form 30 July 2024; Accepted 3 August 2024
Available online 5 August 2024

built-in heat sources to be charged with temperatures lower than 160 °C. Potassium carbonate (K_2CO_3) was chosen as a potential material for residential heat storage since it met all the criteria. The equilibrium reaction for the gas–solid system involving K_2CO_3 can be expressed in (1):

$$K_2CO_3(s) + 1.5H_2O(g) \rightleftharpoons K_2CO_3 \cdot 1.5H_2O(s) + 1.5\Delta H_r \quad (1)$$

where ΔH_r is the reaction enthalpy of 65.8 kJ/mol_{water} [7,8]. During the hydration or discharging process, K_2CO_3 uptakes H_2O to produce $K_2CO_3 \cdot 1.5H_2O$. On the other hand, the right-to-left reaction (dehydration or charging) is endothermic, requiring the addition of heat to release water vapor [9]. Ideally, it is preferable for salt hydrates to undergo the dehydration process at temperatures below 100 °C. This is because such temperatures are more practical for the majority of solar thermal collectors, particularly during periods of reduced sunlight [10].

An important challenge in salt hydrates is the caking phenomenon, resulting from the agglomeration of powdered salt hydrates. The caking process is divided into three distinct stages; moisture sorption, formation of a liquid bridge, and development of a crystal bridge [11]. This agglomeration process gives rise to barriers that impede the mobility of water vapor molecules within the reactor. The presence of these obstructions has the potential to block the water vapor pathways, thereby reducing the overall efficiency of the heat storage mechanism. Therefore, an extra manufacturing step to transform powdered materials into well-defined millimeter-sized granules is essential. Failing to do so can lead to substantial pressure drops across the thermochemical reactor bed, primarily caused by poor diffusion and bed flowability. Consequently, this results in a diminished power output from the reactor bed [12].

Larger granules are expected to improve system performance by providing better flowability within the thermochemical reactor bed [13]. Aarts et al. [14] conducted an investigation into the hydration kinetics of millimeter-sized K_2CO_3 particles with a disk shape. According to their results, tortuosity and particle density (porosity) have a major impact on the hydration kinetics of millimeter-sized salt hydrate particles, with diffusion acting as the main limitation. It is interesting to note that particle performance was largely unaffected by the initial powder size.

Despite of several advantages, large particles can also have some drawbacks. Previous research by Shkatulov et al. [13] demonstrated that irregularly shaped granules, particularly in the case of vermiculite-stabilized K_2CO_3 composites, led to poor packing, resulting in a significant reduction in volumetric storage density. Additionally, the process of converting powder into larger, well-defined particles can potentially lead to a reduction in material performance, primarily due to potential diffusion limitations. To address this issue, porous materials can be used, which have attracted substantial attention across different areas such as CO_2 capture [15], filtration membranes [16], catalyst supports [17], adsorbents [18], and thermal energy storage [19].

To tackle the issues related to pressure drops and diffusion limitations, developing porous K_2CO_3 granules is proposed using the wet granulation technique for the first time. This approach involves mixing K_2CO_3 with potassium bicarbonate ($KHCO_3$) as a pore former, and then subjecting the mixture to a calcination process. There are various pore formers such as carbon black [20], starch [21] or specific polymers [22] that burn off during calcination, resulting in a porous structure. However, these alternatives might introduce impurities or necessitate extra steps to remove by-products. $KHCO_3$ is particularly suitable because it perfectly aligns with our objective of producing pure K_2CO_3 granules with the desired porosity, without any contaminants. As demonstrated in Eq. (2), heating $KHCO_3$ to a specific temperature converts it into K_2CO_3, along with the release of carbon dioxide (CO_2) and water vapor (H_2O):

$$2KHCO_3(s) \rightleftharpoons K_2CO_3(s) + CO_2(g) + H_2O(g) \quad (2)$$

The byproducts are expelled from the granule, creating pores [23]. Consequently, this produces porous K_2CO_3 granules with 100% purity and no additives affecting the energy density, which can be used in thermochemical heat storage and also in CO_2 capture applications [24,25]. Furthermore, the study explores how varying the amount of $KHCO_3$ used for pore formation influences the pore structure, hydration kinetics, and the granules' compression properties. These aspects were systematically optimized to improve the performance and functionality of the final product.

2. Theory

Hydration kinetics of mm-sized salt hydrate particles is mostly limited by the intraparticle diffusion and the key factors that determine the efficiency of this process are the density (porosity) and tortuosity of the particles [14]. In the hydration process of salt hydrate granules, it is assumed that the diffusion through macropores is the rate limiting factor, whereas micropore diffusion and sorption are considered to be fast. At low pressures, Knudsen diffusion occurs in macropores when the mean free path of gas molecules becomes equal to or greater than the size of the pore. This form of diffusion takes place within larger pores or spaces, where gas molecules penetrate the porous structure by means of infrequent collisions with the walls of the pores, rather than by conventional bulk diffusion [26]. The mean free path (λ) of gas molecules is determined by Eq. (3):

$$\lambda = \frac{k_B T}{\sqrt{2}\pi d^2 p} \quad (3)$$

where λ (m) denotes the mean free path of the gas molecules, k_B represents Boltzmann's constant of 1.38×10^{-23} (J/K), $T(K)$ denotes the absolute temperature, d (m) indicates the diameter of the gas molecules, and p (Pa) represents the pressure of the gas. This equation represents the mean free path of a gas molecule, which is the average distance it travels before colliding with other molecules in the gas, given specified temperature and pressure conditions. The adsorption or desorption curve for diffusion controlled solids under conditions of constant diffusivity (in the Henry's law regime or for a small differential concentration change) is expressed as Eq. (4) [27]:

$$\frac{m_t}{m_\infty} = 1 - \frac{6}{\pi^2}\sum_{n=1}^{\infty}\frac{1}{n^2}\exp\left(-\frac{n^2\pi^2 D_e t}{R_p^2}\right) \quad (4)$$

where $\frac{m_t}{m_\infty}$ represents the fractional uptake, which is the ratio of the total quantity adsorbed after time t (m_t) to the total amount adsorbed at equilibrium (m_∞). The variables R_p and D_e refer to the granule radius and effective diffusion coefficient, respectively. In this equation, it is assumed that the particle shape is similar to a sphere with radius R_p and that the pressure step is small enough to allow the diffusivity to remain essentially constant. Eq. (4) maintains a reliable approximation even for different shapes, as long as R_p is interpreted as the radius of a sphere that has the same surface-to-volume ratio as the particle being analyzed [28–30]. In the initial region ($0.1 < m_t/m_\infty < 0.5$), this simplifies to Eq. (5):

$$\frac{m_t}{m_\infty} = \frac{6}{R_p}\sqrt{\frac{D_e t}{\pi}} \quad (5)$$

Therefore, slope of fractional uptake vs. time plot is useful for determining effective diffusion coefficient of granules. Assuming that internal diffusion controls the diffusion rate, the quantification of the diffusion characteristics are investigated for macroporous granules. Conversion or the degree of reaction is another important factor that provides valuable insights into the extent of hydration and the kinetics of the reaction. It is defined as the ratio of the local water content in the material (loading) to the maximum theoretical loading that the material can uptake, which can be calculated by Eq. (6):

$$\alpha_{exp}(t) = \frac{m(t) - m(t_0)}{m(t_f) - m(t_0)} \quad (6)$$

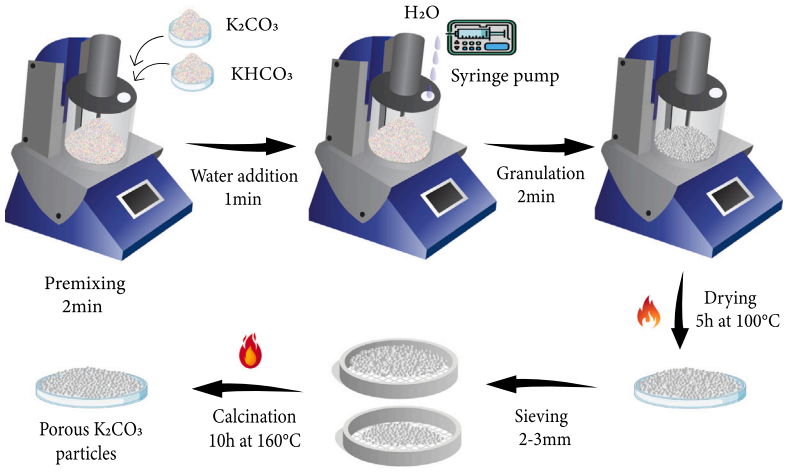

Fig. 1. Schematic of the granulation process, followed by drying at 100 °C for 5 h, sieving, and calcination at 160 °C for 10 h for production of porous K_2CO_3 granules.

where t_f and t_0 are the final and initial times of the hydration according to the thermogravimetry analysis, and $m(t_f)$ and $m(t)$ are the final mass and the mass at time t, respectively. Based on the determined values, the reaction conversion rate ($d\alpha_{exp}/dt$), can be computed for each time point using the first-order backward finite difference approach.

3. Experimental

3.1. Manufacturing granules

The granulation process involved the mixture of potassium carbonate (99%, Thermo Fisher Scientific) and potassium bicarbonate (99.5%, Thermo Fisher Scientific) in a high shear mixer (Eirich EL1) in varying weight ratios of 0, 10, 20, 40, 50, and 60% of the entire batch, represented as K_2CO_3, K10, K20, K40, K50, and K60, respectively. The mixer is equipped with a pin-type rotor located in the center of the vessel and a wall scraper fixed to the top lid. The mixing pan rotated clockwise, while the stirring rotor turned counterclockwise. A schematic of the procedure is illustrated in Fig. 1. The premixing stage involved the mixing of 300 g of the powder mixture at a pan speed of 1.4 m/s, with the rotor speed of 10 m/s for a duration of 2 min. Subsequently, varying quantities of water (Table 1) were added using a syringe pump over a period of 1 min and rotor speed of 5 m/s to facilitate the granulation process. Then, the granulation step commenced, wherein the rotor speed was increased to 10 m/s, and the granulation process continued for a duration of 2 min. Following the granulation step, granules were dried in a hot air oven at 100 °C for 5 h, and then the resulting granules were subjected to sieving, focusing on the size range of 1–5 mm. Finally the granules were calcinated at 160 °C with a heating rate of 1 °C/min for 10 h in a convection oven.

3.2. Characterization of composition and structure

High-temperature X-ray diffraction (D8 Discover, Bruker) equipped with a temperature-controlled heating chamber was used to assess the changes in the crystallographic phase as the sample was heated. The sample was exposed to monochrome Cu-Kα (40 kV, 20 mA), and the 2θ value was varied from 26 to 48°, with a step size of 0.05°, and scanning time steps of 1 s. The sample was heated in the stepwise isothermal heating mode from room temperature to 160 °C, during which isothermal holding steps of 15 min were applied for every 10 °C rise in temperature in the range of 100–160 °C. The morphology of granules was analyzed using a field emission scanning electron microscope (FESEM, JSM-7200F, Jeol) at an accelerating voltage of 5 kV. Before imaging, the sample was fixed to the sample holder using carbon stick tape and then coated with a layer of gold using sputter-coating. Nitrogen adsorption isotherms were collected using a Micromeritics Gemini VII adsorption apparatus. Prior to starting the experiment, the sample underwent outgassing at 160 °C for 3 h.

3.3. Characterization of pore structures

Pore structure of granules was analyzed by ZEISS Xradia Context micro computed tomography (micro-CT). All specimens were scanned in a dry state under the ambient condition. The samples were carefully fixed within a glass tube with a 4 mm diameter, fixed to a small horizontal holder, and precisely centered within the field of view. To absorb moisture, silica gel particles were placed in the lower section of the tube. To generate high-quality images that effectively displayed the features of interest, the following parameters were consistently applied for all scans: 60 kV/5 W power, LE3 filter, an exposure time of 4 s, 10 number of frames, frame averaging (set at 1), a full 360° rotation, and 4016 projections. By setting the source and sample locations, a voxel size of 1.5 μm was achieved. The scanning process started with an initial 30 min warm-up period to ensure instrument stability. Pore analysis was carried out by Dragonfly software developed by Object Research Systems. In this regard, a Volume of Interest (VOI) was defined within the granule structure. This VOI was spherical in shape (2 mm in diameter) and excluded the superficial regions of the specimen that might have been affected by the specimen treatment. The percentage of pores accessible from the surface (open pores) versus those located in the inaccessible interior (closed pores) was determined. This was achieved by creating a shell-like region along all edges of the VOI.

3.4. Density and porosity measurements

Granule density was determined by dividing the granule mass by the volume, which was measured using micro-CT. According to Eq. (7), the relative density can be calculated by dividing the measured density by the theoretical crystal density, which is 2.18 g/cm^3 for hydrated K_2CO_3 and 2.43 g/cm^3 for anhydrous K_2CO_3 [14]. The formula for relative density (ρ_{rel}) is given as:

$$\rho_{rel} = \frac{\rho_{measured}}{\rho_{theoretical}} = 1 - \epsilon \tag{7}$$

In this equation, ρ_{rel} represents the relative density, $\rho_{measured}$ is the measured density, $\rho_{theoretical}$ is the theoretical crystal density, and ϵ is porosity.

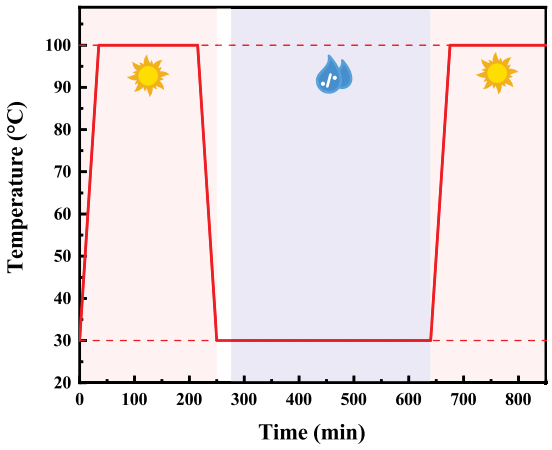

Fig. 2. Temperature program of STA during hydration and dehydration.

Table 1
Water amounts added during granulation.

Sample	Water amount (%)	Remark
K_2CO_3	21	Fine granules
	23	Successful
	25	Powder dissolved
K10	20	Fine granules
	22	Successful
	24	One big chunk
K20	19	Fine granules
	21	Successful
	23	One big chunk
K40	17	Fine granules
	18	Successful
	19	Several big chunks
K50	15	No granulation
	16	Successful
	17	Watery paste
K60	11	No granulation
	12	No granulation
	13	Watery paste

3.5. Simultaneous thermal analysis

Simultaneous thermal analysis (STA) was carried out on granules using a simultaneous thermal analyzer NETZSCH STA 449 F3 Jupiter instrument connected to the ProUmid humidifier system. Decomposition of $KHCO_3$ at different temperatures of 120, 140, and 160 °C in 5 h with a heating rate of 1 °C/min was evaluated by thermogravimetric (TGA) and derivative thermogravimetric (DTG) analysis. To study the hydration kinetics, one granule from each composition with a mass of around 15 mg was placed within an alumina crucible without lid. The specimen underwent initial dehydration at 100 °C with a heating rate 2 °C/min at a constant flow rate of 300 mL/min under dry air atmosphere for 3 h. Subsequently, it was cooled down to a temperature of 30 °C with a cooling rate 2 °C/min and was maintained at this temperature for 30 min to equilibrate. Then, the hydration process was performed for 6 h, during which the water vapor pressure of 13 mbar was supplied. The subsequent dehydration process was carried out under conditions of zero water vapor pressure and a temperature of 100 °C for 3 h. Fig. 2 shows the applied temperature program during hydration and dehydration. To investigate the cyclic performances, the K_2CO_3, K40 and K50 granules with approximate mass of 15 mg were subjected to TGA and DSC measurements for a total of 10 hydration/dehydration cycles. Hydration steps were carried out at 30 °C and 13 mbar for 6 h, while dehydration steps were performed at 100 °C and 0 mbar for 3 h. In each cycle, the loading amount was the ratio of the water mole increase during hydration to mole of the dried sample.

3.6. Compression behavior

Compression tests were conducted on 20 specimens per each batch using a Zwick Z01 at a compressive load speed of 0.1 mm/min. The average of maximum compressive loads was calculated based on the Weibull distribution using Origin software.

4. Results and discussion

4.1. Optimization of granulation process

The wetting and binding properties of the powder particles are significantly affected by the water amount added to the granulation process, thereby influencing granule formation. By maintaining an appropriate water amount, the particles can agglomerate and form cohesive granules. To find the optimum amount of water for successful granulation of pure K_2CO_3, different amounts of 21%, 23%, and 25% relative to the total weight of powder was tested. The water amount significantly impacts the size and density of the resulting granules. Higher water amount tends to yield larger and less dense granules, while lower water amount leads to smaller and denser granules. Addition of 21% water resulted in 48.4% of granules being less than 1 mm in size, suggesting that this water amount was insufficient for the formation of larger granules. Increasing the water amount to 23% of the total powder weight decreased the fraction of granules smaller than 1 mm and yielded in formation of 26.6% granules in 2–3 mm size range. However, the addition of 25% water led to the formation of a large agglomerate without proper granulation. Consequently, 23% water was selected as the optimal amount for successful granulation in subsequent experiments.

In the next stage, K_2CO_3 was mixed with varying weight proportions of $KHCO_3$ (10%, 20%, 40%, 50%, and 60% of the total 300 g batch). The optimal water amount for granulating K_2CO_3 was determined to be 23%. However, when incorporating $KHCO_3$, the required water amount reduced, due to its higher hygroscopicity than K_2CO_3. Table 1 shows the water amounts added to each composite and related remarks regarding the granulation process. Additionally, Fig. S1 represents the final shapes of materials in the granulator pan after the granulation process with different amounts of water added to each batch. Successful granulation for K_2CO_3, K10, K20, K40, and K50 was achieved using 23%, 22%, 21%, 18%, and 16% water, respectively. Attempts to granulate K_2CO_3 with 60% $KHCO_3$ using 11, 12, and 13% water failed and no granules formed. This indicates that the highest possible amount of pore former for achieving successful granulation is around 50%. The limitation on the quantity of $KHCO_3$ that prevents granule formation is due to the hygroscopic properties of these compounds. $KHCO_3$ is more hygroscopic than K_2CO_3. This means that $KHCO_3$ tends to absorb more moisture from the environment. When the proportion of $KHCO_3$ is too high, the mixture may become too moist, preventing the formation of strong bonds between granules.

Fig. 3a presents histograms of granule size determined by sieve analysis. Fig. 3b depicts the final calcinated 2–3 mm granules after successful granulation with optimum water amounts. In all cases, the granules with size range 2–3 mm exhibited the highest yield. Furthermore, this range of granule diameters offers a comparative balance between inter-particle and intra-particle mass transfer. Schaefer and Thess, [31] reported that the diameter of adsorbent granules has a significant impact on its degree of discharging and the optimal granule diameter range is about 2–4 mm to reach maximum degree of discharge. This optimum is attributed to the balance of mass transfer resistances. In smaller diameters, the discharging degree is limited by the inter-particle mass transfer, and in larger diameters, the limitation comes from within the particles themselves, limited by intra-particle mass transfer.

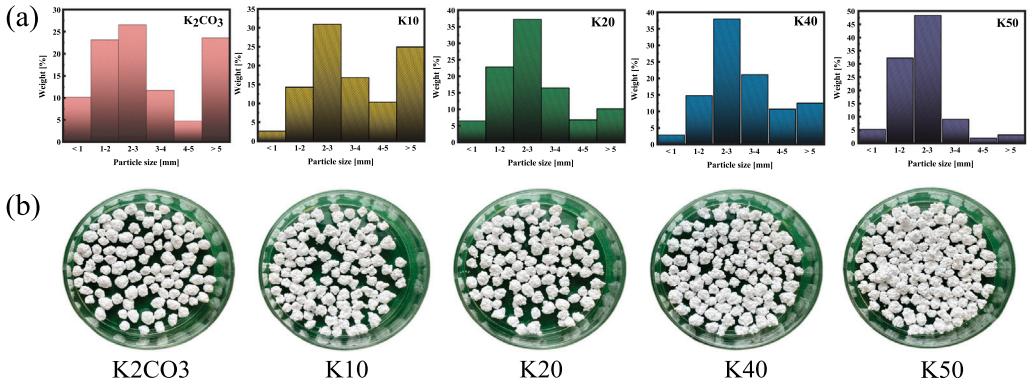

Fig. 3. (a) Histograms of granule size determined by sieve analysis for K_2CO_3, K10, K20, K40, and K50 granules. (b) Images of calcinated 2–3 mm granules after successful granulation with optimum water amounts.

4.2. Analysis of composition and morphology

Due to the highest amount of $KHCO_3$ in K50, this sample was selected for XRD measurement to clearly show the changes of XRD patterns during stepwise isothermal heating (Fig. 4a). The crystalline phase transition from $KHCO_3$ to K_2CO_3 started between 110 and 120 °C under stepwise isothermal heating. The $KHCO_3$ peaks (ICSD 2325 [32]) at 30.4, 31.2, and 37.2°, then started to decrease, which was compensated by a gradually rising K_2CO_3 diffraction peaks (ICSD 52535 [33]) at 33.7, 37.5, 39.38, and 43.8°. The $KHCO_3$ to K_2CO_3 transition produced no distinguishable intermediate crystalline phases. According to the XRD data, the sample's entire amount of $KHCO_3$ was converted to K_2CO_3 at 160 °C, and nothing else changed after this temperature.

Calcination of $KHCO_3$ powder at temperatures 120, 140, and 160 °C with heating rate 1 °C/min was also observed by thermogravimetric (TGA) and derivative thermogravimetric (DTG) curves in Fig. 4b and Fig. 4c. During the calcination process, $KHCO_3$ decomposed to K_2CO_3, CO_2 and H_2O, as described by Eq. (2). This decomposition was evidenced by 31% (± 0.1%) mass reduction after 530, 180, and 100 min heating at temperatures of 120, 140, and 160 °C, respectively. Since the theoretical weight loss expected from Eq. (2) is 31%, it indicates that the decomposition was complete.

The decomposition temperature can affect the size of the resulting pores [34]. To examine how the decomposition temperature affects pore size, $KHCO_3$ was heated to 120, 140, and 160 ° C for 5 h at a rate of 1 °C/min. According to the SEM images in Fig. S2(a–c) and pore size distributions in Fig. S2(d–f), as the decomposition temperature increased from 120 to 160 °C, the pore size range increased from 0.198 ± 0.08 μm to 0.223 ± 0.08 μm. To measure how much $KHCO_3$ really exists in K50 granules, thermogravimetric analysis was carried out by placing three granules in the crucible of the STA. Initially, the granules were dried at 70 °C for 5 h to remove absorbed water during the granulation. Then the calcination was done at 160 °C for 5 h with heating rate 10 °C/min. According to Fig. 4d, the mass loss amount during calcination corresponds to the existence of 55% $KHCO_3$ in K50 granules. This explains that the difference in amount of initially added and final $KHCO_3$ in K50 granules is only around 5%.

Fig. 5a–e displays the FESEM images of the granules. The K_2CO_3 granule exhibited a compact structure (Fig. 5a), but as the amount of pore former increased, macropores emerged within the granule. When 20% or more of the pore former was added, cracks were observed near the macropores due to the burnout of the pore former. When CO_2 and H_2O gases escape from the material, they create pressure within the granule. The buildup of this pressure can induce the formation of cracks as the gases try to find a path out from the granule. Furthermore, the calcination process induces both physical and chemical transformations in potassium bicarbonate, which in turn result in changes to its structure, ultimately leading to the formation of cracks. The escaping of gases, in conjunction with these changes in structure, leads to the development of cracks in the substance. When the amount of pore former reached 50%, a greater amount of burnout gases attempted to escape as the material decomposed (Fig. 5e). This increased the pressure buildup and led to more crack formation within the material during calcination. Although these cracks may weaken the granule, they facilitate the water vapor transfer within the granule, hence enhancing the diffusion kinetics. Fig. S3 displays a cross-sectional FESEM image of a K50 granule. The image clearly illustrates the architecture of a significant cavity, clearly outlining its walls that contain numerous macropores. This visualization provides a comprehensive understanding of the complex network of macropores within the voids.

4.3. Analysis of the porous structures

Micro-CT analysis of granules with different proportions of pore former revealed notable distinctions in their structural properties, porosity, and density in Fig. 5f–j. Table 2 provides a detailed data on the volume, density, and porosity of each whole granule. Supplementary Movie 1 represents the animation of sequential slices through the granules. K_2CO_3 granule without pore former is a compact and homogeneous structure featuring small dispersed pores throughout the material. The absence of a pore former led to minimal void spaces within the material, yielding the recorded porosity of 26% and the highest density (1.797 g/cm^3) among all the anhydrous granules.

Fig. 5g revealed the presence of numerous large pores within the K10 granule. The introduction of a small amount of pore former into a dense granule obstructed the exit pathways for CO_2 and H_2O gases released during the calcination. Consequently, the pressure to escape resulted in the formation of these large pores. These pores could act as stress concentrators, potentially decreasing the mechanical stability of the granules. The K20 granule exhibited a porous structure and enhanced pore interconnectivity compared to the K10 granule, facilitating more efficient gas transfer during calcination. Given the higher porosity of 31%, the density of this granule was measured at 1.685 g/cm^3. The K40 granule in Fig. 5i exhibited a porous structure with extensive pore interconnections, resulting in a density of 1.560 g/cm^3 and a porosity of 33%. The K50 granule in Fig. 5j exhibited a highly porous structure with numerous large void spaces. This granule demonstrated the highest porosity of 40% and the lowest density at 1.456 g/cm^3 among all the samples, indicating that a substantial portion of its volume was occupied by pores. It is worth noting that while the large pores in the K50 structure facilitated mass transfer, they also posed a potential challenge to the mechanical stability of the granule.

For pore analysis using Dragonfly software, a spherical volume of interest (VOI) with 2 mm in diameter was defined within the granule to exclude the sample edges that might have been affected by the sample treatment. Fig. 5k-o and Supplementary Movie 2 show the spherical

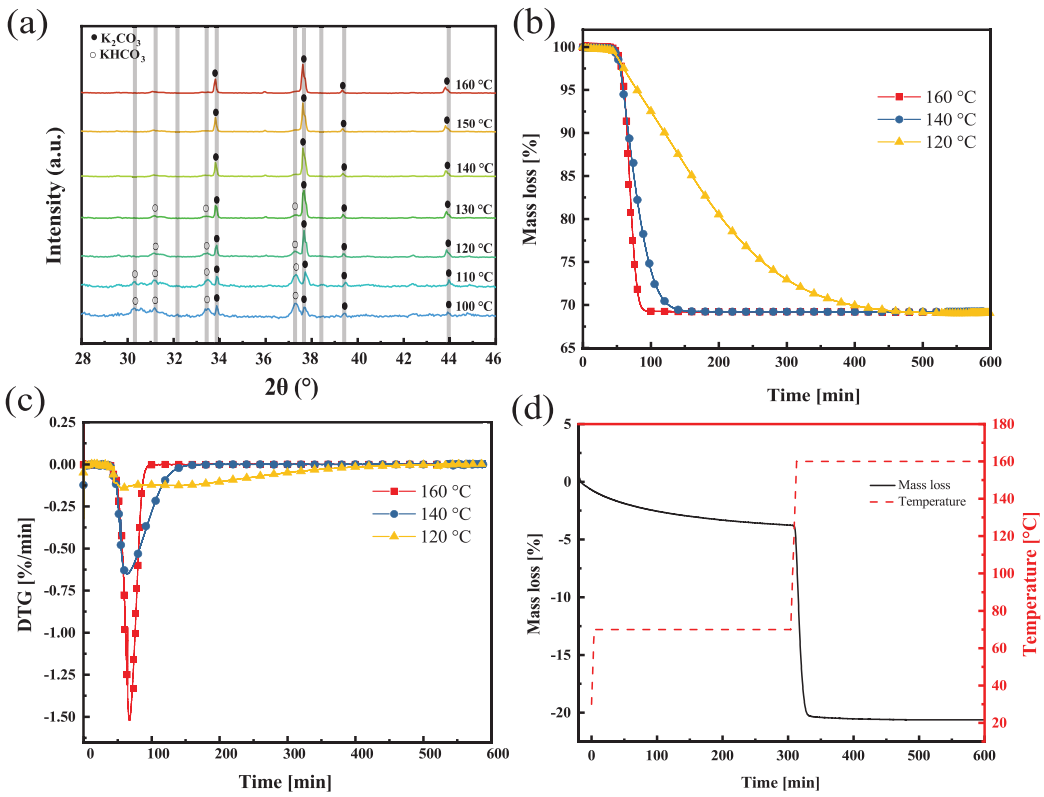

Fig. 4. (a) Changes in the XRD pattern of the K50 sample while heated according to the stepwise isothermal heating program. (b) Thermogravimetric and (c) derivative thermogravimetric curves of $KHCO_3$ powder during the calcination at temperatures 120, 140, and 160 °C with heating rate 1 °C/min. (d) Thermogravimetric analysis of K50 during initial drying at 70 °C for 5 h and calcination at 160 °C for 5 h with heating rate 10 °C/min.

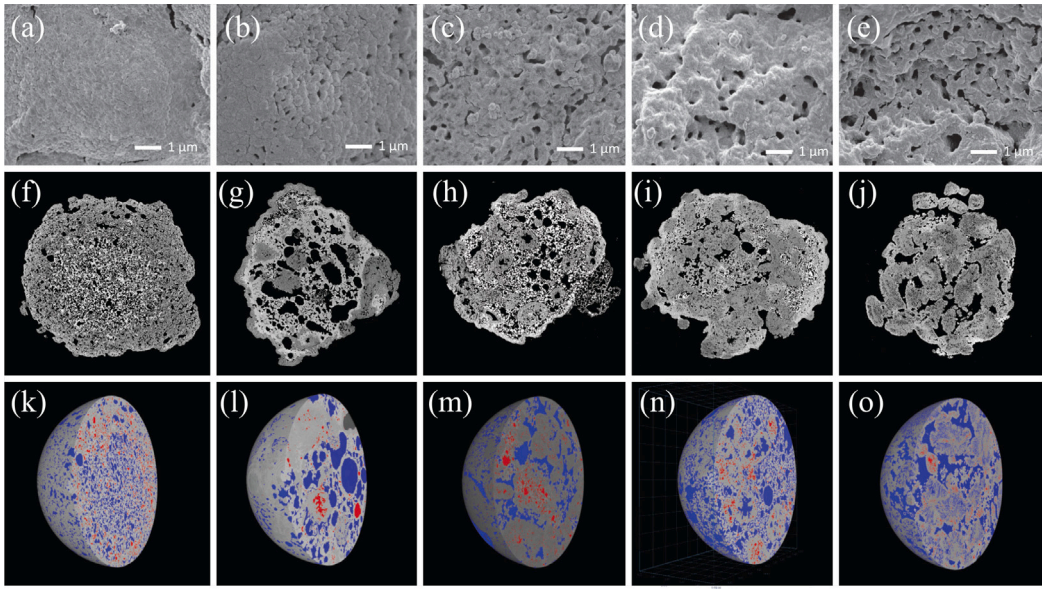

Fig. 5. FESEM images of (a) K_2CO_3, (b) K10, (c) K20, (d) K40, and (e) K50 granules after the calcination at 160 °C for 5 h. Micro-CT images of the entire (f) K_2CO_3, (g) K10, (h) K20, (i) K40, and (j) K50 granules. Pore analysis in 2 mm diameter spherical VOI within the (k) K_2CO_3, (l) K10, (m) K20, (n) K40, and (o) K50 granules. Open and closed pores are depicted in blue and red colors, respectively.

VOI images and the animations of sequential slices through spherical VOIs, respectively. The pores accessible from the surface (open pores) are depicted in blue, while those located in the inaccessible interior (closed pores) are depicted in red. Porosity analysis of granules revealed insightful information on open, closed, and total porosity, represented in Table 3. As the quantity of pore former increases, there is a corresponding rise in the open porosity. Conversely, the volume of closed porosity exhibits a decline. The porosity values derived from the pore analysis in the spherical VOI are slightly lower than those calculated using Eq. (7). This difference can be attributed to the approach of utilizing a spherical volume of interest with a diameter of 2 mm as opposed to considering the entire granule in order to mitigate the impact of edges. This discrepancy can be also due to the voxel size used during scanning. Specifically, the voxel size was 1.5 μm, meaning

Table 2
Pore analysis data from Micro-CT, considering the whole anhydrous granules.

Sample	K_2CO_3	K10	K20	K40	K50
Mass (mg)	16.48	15.88	15.82	15.85	16.44
Volume (mm^3)	9.17	9.42	9.78	10.16	11.29
Density (g/cm^3)	1.797	1.685	1.617	1.560	1.456
Porosity (–)	0.26	0.31	0.33	0.36	0.40

Table 3
Pore analysis data from Micro-CT, considering a 2 mm diameter spherical VOIs within the granules.

Sample	K_2CO_3	K10	K20	K40	K50
Open porosity	0.198	0.212	0.266	0.297	0.303
Closed porosity	0.046	0.021	0.018	0.014	0.011
Total porosity	0.244	0.233	0.284	0.311	0.322

that pores smaller than this size cannot be detected. Consequently, the software analysis may underestimate porosity due to its inability to capture these smaller void spaces. Although there was a minor variance in the total porosity calculated using two methods, there is a consistent trend in the open and closed porosity measurements and with increasing the amount of pore former, open porosity enhanced (Table 3).

4.4. Hydration kinetics and heat storage performance

The presence of macroporosity was analyzed with nitrogen adsorption isotherms. According to the IUPAC classifications [35], the adsorption isotherm of K50 adhered to type-III isotherm. Fig. 6a illustrates that nitrogen adsorption took place at a high relative pressure ($p/p_0 > 0.9$). The type III isotherm has a concave shape without any inflection point. This occurs when the interactions between adsorbed molecules are stronger than the interactions between the adsorbent surface and the adsorbate [36,37]. This indicates the isotherm behavior typical of macroporous materials.

The conversion plots in Fig. 6b provide important insights into the extent of hydration over reaction time for all granules. Initially, the conversion starts at zero, indicating absence of reaction between potassium carbonate and water vapor. As the reaction proceeds, an initial rapid rise is observed followed by a slower increase as the reaction is near completion. The plateau on the conversion plot indicates equilibrium in the hydration reaction, with no further water uptake, which was observed only for K50 granule. The presented figure demonstrates that over a 6-h hydration period, the conversion degrees for K_2CO_3, K10, and K20 granules reached 0.17, 0.23, and 0.41, respectively, all of which are lower than the conversion degree of 0.77 observed for K_2CO_3 powder. Notably, conversion degrees for K40 and K50 reached 0.87 and 1, respectively, signifying superior water vapor mass transfer within these granules.

Fig. 6c shows the conversion rate versus time plots for various granules over a 6-h hydration period, indicating that the hydration rate accelerates as the amount of pore former increases. In the hydration process of granules, there was an initial rapid increase in mass, followed by a gradual transition to a slower hydration phase where the mass increment occurred at a significantly reduced rate. The overall transformation of a reactant into products can sometimes include multiple stages, each with its own distinct extent of conversion [38]. By examining conversion rate-time plots, it was evident that all granules underwent a two-step hydration process [39,40]. The initial stage of the process involves the hydration reaction of a outer layer of the granule, resulting in rapid reaction kinetics and a linear relationship of conversion rate over time, which indicates that the response is either first-order or very close to being first-order [38]. Following the initialization period, the subsequent diffusion phase commences. During this stage, the outer layer of the granule, which is fully hydrated, diffuse inward as the hydration progresses [41]. In the phase controlled by diffusion, the rate of product formation decreases proportionally with an increase in the thickness of the product layer, which, in our context, corresponds to hydrated K_2CO_3. Eventually, this conversion rate reaches zero, indicating that the reaction has reached a point where it no longer advances further.

Table 4
Effective diffusion coefficient of granules computed using Eq. (5).

Sample	D_e [m^2/s]	R^2
K_2CO_3	2.290×10^{-13}	0.9924
K10	2.123×10^{-13}	0.9584
K20	1.130×10^{-12}	0.9878
K40	8.475×10^{-12}	0.9995
K50	4.271×10^{-11}	0.9935

To calculate the effective diffusion coefficient of granules, linearization technique of uptake curves was implemented. Fig. 6d demonstrates that when $0.1 < m_t/m_\infty < 0.5$ and the hydration front has not yet reached the granule center, the quantity of adsorbate is directly proportional to the square root of time. Considering granules with diameter of 3 mm, Eq. (5) is employed to get the effective diffusion coefficients based on the slope of these linear graphs, which are presented in Table 4 and Fig. 6e. The linearity of the graphs was demonstrated by the coefficient of determination (R^2), which approached a value of 1. The K50 and K40 granules exhibited a notable increase in the effective diffusion coefficients with values 4.271×10^{-11} and 8.475×10^{-12} m^2/s, respectively. This means that water vapor molecules travel, on average, 186 and 37 times faster in these granules compared to K_2CO_3 granule with a diffusion coefficient of 2.290×10^{-13} m^2/s. The mean free path of a water vapor molecule was determined using Eq. (3). At the applied pressure, the water vapor molecules have a mean free path of around 10 μm, that is at least 20 times greater than the typical macropores radius. Therefore, the transportation via the macropores is mostly caused by Knudsen flow or Knudsen diffusion.

4.5. Compression behavior

The presence of pores in the materials leads to crack tip blunting, which occurs when a crack comes into contact with a pore. This blunting reduces the length of the crack and enhances the material's fracture toughness [42]. Fig. 6f demonstrates the average of maximum compressive load for 20 specimens per batch based on Weibull distribution with derivation of 95% confidence intervals (95%CI) using Origin software. K_2CO_3 demonstrated the highest maximum compressive load, whereas K10 and K50 presented the lowest values. As represented in Fig. 5g and Fig. 5j, existence of large voids in these granules functioned as stress concentrators and decreased the maximum compressive load values. The maximum compressive load demonstrates the superior compression characteristics of the K20 and K40 granules. Taking into account the volume changes during hydration and dehydration, a dense granule tends to crack immediately after fewer cycles. In contrast, a porous material undergoes gradual cracking and ultimately breaks after a greater number of cycles. This underscores the significance of using porous materials in thermochemical heat storage systems [43].

4.6. Cyclic heat storage performance

To investigate the cyclic performance and reaction reversibility, the K_2CO_3, K40 and K50 granules were subjected to TGA and DSC measurements for 10 hydration and dehydration cycles. The hydration and dehydration reactions both proceeded in a single step, and no double salt formation during the hydration was observed [44]. The extent of hydration/dehydration of K_2CO_3, K40, and K50 granules are shown in Fig. 7a. The loading, expressed in $mol_{H_2O}/mol_{K_2CO_3}$, was measured across multiple cycles. K_2CO_3 displayed slow hydration

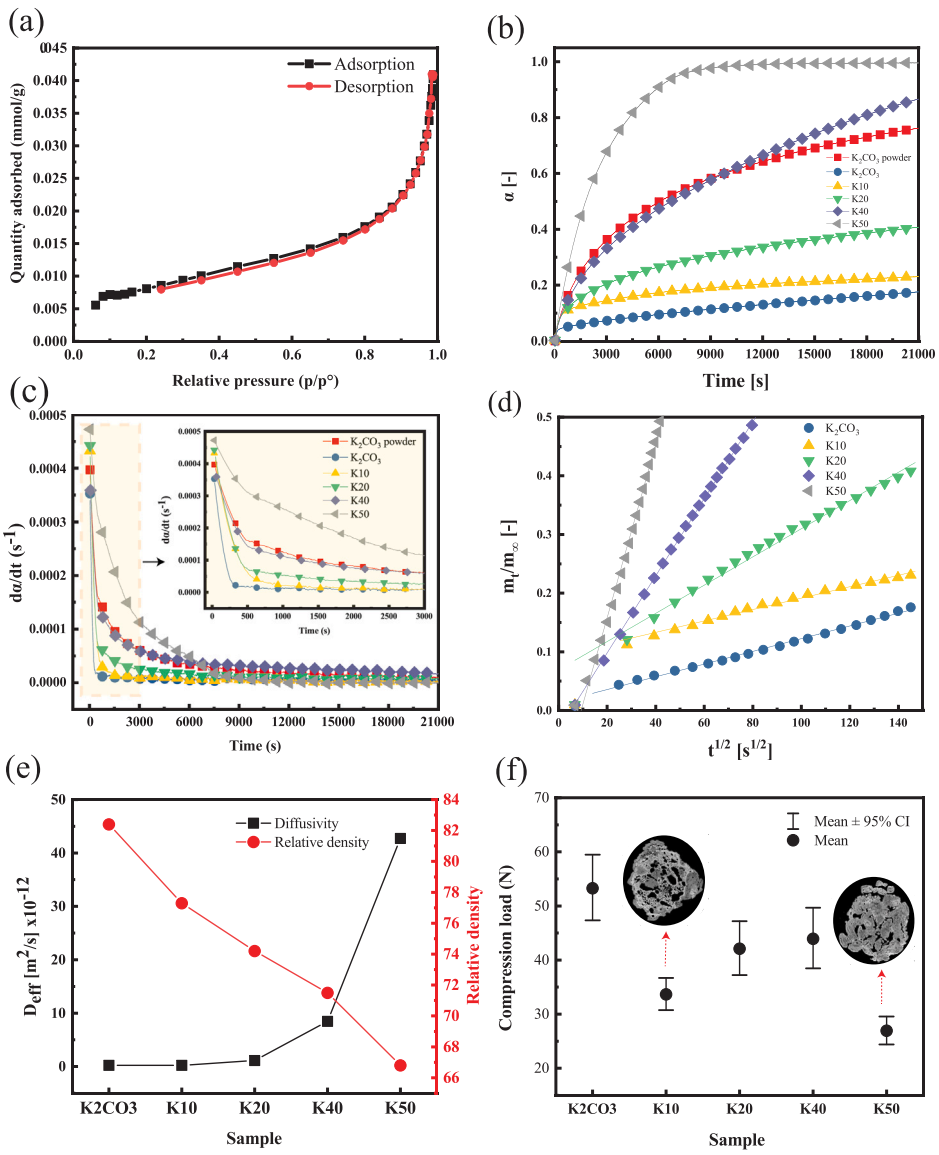

Fig. 6. (a) Nitrogen adsorption/desorption isotherms of K50 under different relative pressures. (b) Conversion (c) and conversion rate vs. time plots of granules with approximate mass of 15 mg at hydration temperature of 30 °C and water vapor pressure of 13 mbar. (d) Fractional uptake profiles in the short time domain of granules. (e) Effective diffusion coefficient of granules. (f) Average of maximum compressive loads for 20 specimens per batch based on Weibull distribution with derivation of 95% confidence intervals (95%CI).

kinetics with a loading around 0.2 $mol_{H_2O}/mol_{K_2CO_3}$ in the first cycle. Although the hydration kinetics got faster over cycles, K_2CO_3 granule did not reach a complete hydration even in the 10th cycle. Nonetheless, K40 demonstrates a significantly higher hydration loading than K_2CO_3, achieving complete hydration by the 4th cycle. K50 exhibits the fastest reaction kinetics, attaining the highest water loading capacity of 1.5 $mol_{H_2O}/mol_{K_2CO_3}$ from the first cycle. Both K40 and K50 granules maintained consistent loading capacities, indicating strong stability during repeated hydration and dehydration cycles.

Fig. 7b displays the DSC results during the hydration/dehydration processes. Using the Netzsch software, the heat released data during the hydration was computed by integrating the area under each DSC peak, with detailed values provided in Table 5. In K_2CO_3 granule, the heat released during hydration increased progressively with each cycle, starting from 6.3 kJ/mol_{H_2O} in the first cycle to 58.9 kJ/mol_{H_2O} in the tenth cycle. This is associated with the generation of pores and volume changes over cycles, which enhance gas transfer during the hydration and improves the diffusion kinetics. K40 exhibited a higher initial heat release than K_2CO_3, starting at 31.2 kJ/mol_{H_2O} and stabilizing around 59.5 kJ/mol_{H_2O} by the 10th cycle. K50 released 60.7 kJ/mol_{H_2O} in the first cycle and 62.3 kJ/mol_{H_2O} in the tenth cycle. These results emphasize the improved hydration kinetics and stability of K40 and K50 in comparison to pure K_2CO_3. The inclusion of a pore former significantly boosts the hydration and dehydration kinetics, with K50 exhibiting the highest performance among the tested samples.

4.7. Analysis of volumetric energy density

To determine the volumetric energy density (VSD) of K50 in the granule level, the density of the hydrated granule is required. For this purpose, the volume change during the first cycle is considered negligible. Thus, the density of the hydrated granule is calculated by dividing its mass by the volume obtained from micro-CT data. The hydrated K50 granule's density was determined to be 1.74 g/cm^3, which results in a gravimetric energy density of 60.7 kJ/mol. The volumetric energy densities of K50 (in the first hydration cycle) and the theoretical maximum energy density of K_2CO_3 powder are 0.96 and 1.3 GJ/m^3, respectively, demonstrating that the energy density of K50 is around 74% of the theoretical maximum. Micro-CT analysis in Fig. 5f–j and Table 2 showed that K50 has 40% porosity with a smaller bulk density

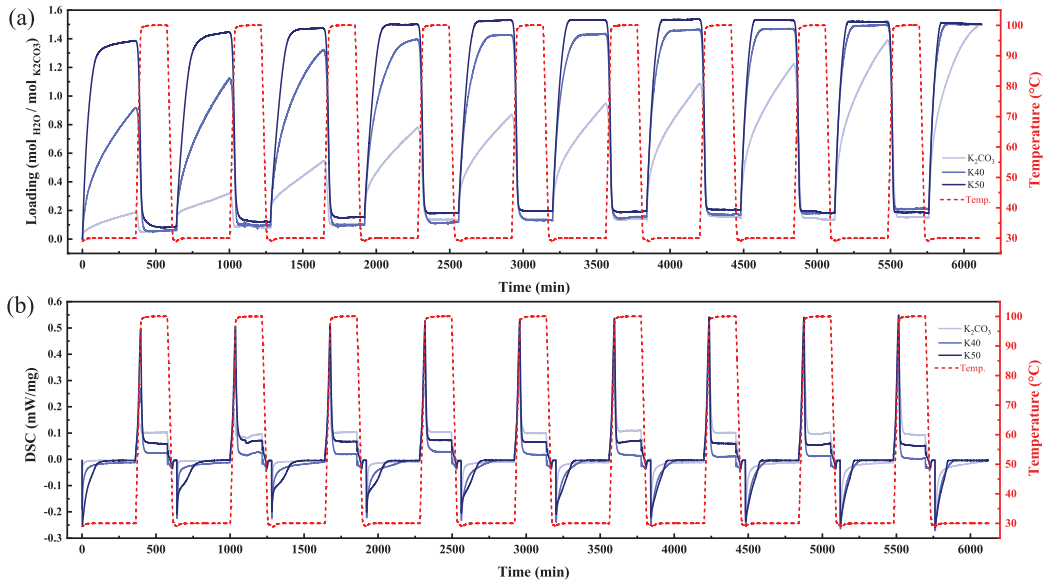

Fig. 7. Cyclic stability measurements of K_2CO_3, K40, and K50 granules over 10 hydration/dehydration cycles. (a) Loading or extent of hydration in the granules over time using the TGA measurement. (b) Recorded heat flow via the DSC measurement. Hydration steps were carried out at 30 °C and 13 mbar for 6 h, while dehydration steps were performed at 100 °C and 0 mbar for 3 h.

Table 5
Heat released during 6h hydration of K_2CO_3, K40, and K50 granules over 10 cycles at 30 °C and water vapor pressure of 13 mbar using DSC measurement.

Cycle	Heat released during hydration (KJ/mol_{H2O})		
	K_2CO_3	K40	K50
1	6.3	31.2	60.7
2	10.6	35.0	61.9
3	18.4	47.5	61.4
4	24.6	59.2	62.6
5	28.1	59.1	61.0
6	31.0	58.9	62.2
7	34.2	60.7	61.5
8	41.0	59.5	62.8
9	45.9	59.1	61.2
10	58.9	59.5	62.3

Table 6
Comparison of the volumetric energy densities (VSD) of the developed K50 granule in this work with other literature studies according to the discharge conditions.

Material	VSD [GJ/m^3]	Discharge condition	Ref.
K50 granule	0.96	13 mbar, 30 °C	This work
K_2CO_3 grains	0.75	13 mbar, 30 °C	[45]
K_2CO_3–Expanded graphite (EG)	0.49–0.77	12 mbar, 25 °C	[46]
K_2CO_3–Vermiculite	0.33	14 mbar, 40 °C	[13]
K_2CO_3-Polymer	0.5	12 mbar, 30 °C	[12]

than K_2CO_3 powder. This indicates that, compared to the powder state, K50 occupies more volume, which results in a decreased volumetric energy density compared to the theoretical maximum energy density of K_2CO_3 powder.

The comparison of VSD of the developed K50 granule with other studies provides insights into the performance of various K_2CO_3-based composite materials. Table 6 summarizes the findings from different studies, allowing us to understand the relative efficiencies of these materials. Gaeini et al. [45] studied K_2CO_3 grains, obtaining a VSD of 0.66 GJ/m^3 under the same conditions. Zhao et al. [46] synthesized a K_2CO_3-based composite material using expanded graphite (EG) and octylphenol polyoxyethylene(10) ether (OP-10). The VSD of their composite material ranged from 0.49 to 0.77 GJ/m^3, depending on the EG and K_2CO_3 contents. Shkatulov et al. [13] prepared a K_2CO_3 composite in expanded vermiculite with 69 wt% of the salt, achieving a VSD of 0.33 GJ/m^3. Aarts et al. [12] used a porous hydrophilic polymeric matrix based on crosslinked poly (hydroxyethyl methacrylate) (pHEMA) to stabilize K_2CO_3 via vacuum impregnation. The VSD of this composite was measured at 0.5 GJ/m^3 under discharge conditions of 12 mbar and 30 °C. In conclusion, the developed K50 granule demonstrates significant advantages over other K_2CO_3-based composite materials reported in the literature. Its superior energy density position it as a promising candidate for energy storage applications. The comparison with existing studies highlights the effectiveness of our approach in preserving energy storage efficiency.

5. Conclusion

In this study, a novel method was developed to synthesize porous K_2CO_3 granules using $KHCO_3$ as a pore former in varying ratios of 10, 20, 40, and 50 wt%. It is important to highlight that the maximum effective amount of $KHCO_3$ for successful granulation is around 50 wt%. Beyond this level, granule formation does not occur. This approach resulted in the formation of porous K_2CO_3 granules that are 100% pure and free from additives that could impact energy density. The K50 and K40 granules showed significant improvements in effective diffusion coefficients compared to K_2CO_3 granules without a pore former. In cyclic performance tests, K_2CO_3 granules without pore former exhibited slow kinetics and incomplete hydration even after 10 cycles. In contrast, K40 and K50 granules demonstrated significantly faster hydration kinetics, with K40 achieving complete hydration by the 4th cycle and K50 reaching a maximum water loading capacity from the first cycle. The K50 granule, with a hydrated state density of 1.74 g/cm^3, achieved a volumetric energy density of 0.96 GJ/m^3. Among the developed granules, K50 exhibited the best hydration kinetics, positioning it as a promising candidate for thermochemical heat storage applications. Despite the K50 granule's superior diffusion kinetics and hydration performance, the presence of numerous large voids served as stress concentrators, thereby reducing its compressive strength. Enhancing the mechanical strength of these granules remains a crucial area for future research, focusing on developing methods to reinforce the structural integrity without compromising their excellent diffusion kinetics and energy density. This study underscored the potential of modifying pore morphology to enhance thermochemical heat storage efficiency and demonstrates that the wet granulation technique could be effectively used for mass production of salt hydrate granules.

CRediT authorship contribution statement

Delaram Salehzadeh: Writing – review & editing, Writing – original draft, Validation, Methodology, Investigation, Formal analysis. **Behrooz Elahi:** Writing – review & editing, Validation, Methodology, Conceptualization. **Johan E. ten Elshof:** Writing – review & editing, Supervision, Methodology, Conceptualization. **Gerrit Brem:** Writing – review & editing, Supervision. **Mohammad Mehrali:** Writing – review & editing, Validation, Supervision, Resources, Methodology, Investigation, Funding acquisition, Formal analysis, Conceptualization.

Declaration of competing interest

The authors declare the following financial interests/personal relationships which may be considered as potential competing interests: Mohammad Mehrali reports financial support was provided by University of Twente. If there are other authors, they declare that they have no known competing financial interests or personal relationships that could have appeared to influence the work reported in this paper.

Data availability

No data was used for the research described in the article.

Acknowledgment

The authors would like to acknowledge the financial support from the Sectorplan techniek and TKI Urban Energy (SALTECH project-TKITOE2021402).

Appendix A. Supplementary materials

Supplementary material related to this article can be found online at https://doi.org/10.1016/j.cej.2024.154560.

References

[1] N. Mazur, M.A. Blijlevens, R. Ruliaman, H. Fischer, P. Donkers, H. Meekes, E. Vlieg, O. Adan, H. Huinink, Revisiting salt hydrate selection for domestic heat storage applications, Renew. Energy 218 (2023) 119331.
[2] T. Uchino, C. Fushimi, Fluidized bed reactor for thermochemical heat storage using Ca (OH) 2/CaO to absorb the fluctuations of electric power supplied by variable renewable energy sources: A dynamic model, Chem. Eng. J. 419 (2021) 129571.
[3] W. Li, J.J. Klemeš, Q. Wang, M. Zeng, Characterisation and sorption behaviour of LiOH-LiCl@ EG composite sorbents for thermochemical energy storage with controllable thermal upgradeability, Chem. Eng. J. 421 (2021) 129586.
[4] T. Yan, T. Li, R. Wang, Thermochemical heat storage for solar heating and cooling systems, in: Advances in Solar Heating and Cooling, Elsevier, 2016, pp. 491–522.
[5] W. Hua, H. Yan, X. Zhang, X. Xu, L. Zhang, Y. Shi, Review of salt hydrates-based thermochemical adsorption thermal storage technologies, J. Energy Storage 56 (2022) 106158.
[6] T. Kousksou, P. Bruel, A. Jamil, T. El Rhafiki, Y. Zeraouli, Energy storage: Applications and challenges, Sol. Energy Mater. Sol. Cells 120 (2014) 59–80.
[7] L. Sögütoglu, P. Donkers, H. Fischer, H. Huinink, O. Adan, In-depth investigation of thermochemical performance in a heat battery: Cyclic analysis of K2CO3, MgCl2 and Na2S, Appl. Energy 215 (2018) 159–173.
[8] E. Washburn, International Critical Tables of Numerical Data, Physics, Chemistry and Technology (1st Electronic Edition), Knovel, 1926 - 1930, 2003.
[9] J. Houben, L. Sögütoglu, P. Donkers, H. Huinink, O. Adan, K2CO3 in closed heat storage systems, Renew. Energy 166 (2020) 35–44.
[10] F. Kuznik, K. Johannes, Thermodynamic efficiency of water vapor/solid chemical sorption heat storage for buildings: Theoretical limits and integration considerations, Appl. Sci. 10 (2) (2020) 489.
[11] M. Chen, S. Wu, S. Xu, B. Yu, M. Shilbayeh, Y. Liu, X. Zhu, J. Wang, J. Gong, Caking of crystals: Characterization, mechanisms and prevention, Powder Technol. 337 (2018) 51–67.
[12] J. Aarts, B. van Ravensteijn, H. Fischer, O. Adan, H. Huinink, Polymeric stabilization of salt hydrates for thermochemical energy storage, Appl. Energy 341 (2023) 121068.
[13] A. Shkatulov, J. Houben, H. Fischer, H. Huinink, Stabilization of K2CO3 in vermiculite for thermochemical energy storage, Renew. Energy 150 (2020) 990–1000.
[14] J. Aarts, S. de Jong, M. Cotti, P. Donkers, H. Fischer, O. Adan, H. Huinink, Diffusion limited hydration kinetics of millimeter sized salt hydrate particles for thermochemical heat storage, J. Energy Storage 47 (2022) 103554.
[15] A. Azmi, M. Aziz, Mesoporous adsorbent for CO2 capture application under mild condition: a review, J. Environ. Chem. Eng. 7 (2) (2019) 103022.
[16] Q. Li, Y. Li, X. Ma, Q. Du, K. Sui, D. Wang, C. Wang, H. Li, Y. Xia, Filtration and adsorption properties of porous calcium alginate membrane for methylene blue removal from water, Chem. Eng. J. 316 (2017) 623–630.
[17] J. Cheng, Y. Wang, C. Teng, Y. Shang, L. Ren, B. Jiang, Preparation and characterization of monodisperse, micrometer-sized, hierarchically porous carbon spheres as catalyst support, Chem. Eng. J. 242 (2014) 285–293.
[18] J. Lupa, K. Morlo, R. Dobrowolski, P. Legutko, A. Sienkiewicz, A. Kierys, Highly porous cerium oxide prepared via a one-step hard template method as an extremely effective adsorbent for arsenic species removal from water, Chem. Eng. J. 474 (2023) 145750.
[19] Z. Wu, C. Zhao, Experimental investigations of porous materials in high temperature thermal energy storage systems, Sol. Energy 85 (7) (2011) 1371–1380.
[20] J. Liu, Y. Li, Y. Li, S. Sang, S. Li, Effects of pore structure on thermal conductivity and strength of alumina porous ceramics using carbon black as pore-forming agent, Ceram. Int. 42 (7) (2016) 8221–8228.
[21] S.G. Aspromonte, M.A. Tavella, M. Albarracín, A.V. Boix, Mesoporous biomaterials synthesized with corn and potato starches applied in CO2 capture, J. Environ. Chem. Eng. 11 (4) (2023) 109542.
[22] Y. Feng, K. Wang, J. Yao, P.A. Webley, S. Smart, H. Wang, Effect of the addition of polyvinylpyrrolidone as a pore-former on microstructure and mechanical strength of porous alumina ceramics, Ceram. Int. 39 (7) (2013) 7551–7556.
[23] H. Luo, H. Chioyama, S. Thürmer, T. Ohba, H. Kanoh, Kinetics and structural changes in CO2 capture of K2CO3 under a moist condition, Energy Fuels 29 (7) (2015) 4472–4478.
[24] D. Rossi, I. Anguillesi, U. Desideri, M. Seggiani, Easy fabrication method of Li4SiO4-K2CO3 based pellets for CO2 capture at high temperature, Chem. Eng. J. 481 (2024) 148615.
[25] C. Ling, Z. Wang, Z. Tang, Performance improvement of Na4SiO4 doped with Li2CO3-K2CO3 for high-temperature CO2 capture and thermochemical energy storage, Chem. Eng. J. 476 (2023) 146921.
[26] G. Youngquist, J.L. Allen, J. Eisenberg, Adsorption of hydrocarbons by synthetic zeolites, Ind. Eng. Chem. Prod. Res. Dev. 10 (3) (1971) 308–314.
[27] H.G. Karge, J. Weitkamp, Adsorption and Diffusion, vol. 7, Springer Science & Business Media, 2008.
[28] J. Kärger, D.M. Ruthven, D.N. Theodorou, Diffusion in Nanoporous Materials, vol. 48, Wiley Online Library, 2012.
[29] J. Kärger, Transport phenomena in nanoporous materials, ChemPhysChem 16 (1) (2015) 24–51.
[30] P. Peng, D. Stosic, A. Aitblal, A. Vimont, P. Bazin, X.-M. Liu, Z.-F. Yan, S. Mintova, A. Travert, Unraveling the diffusion properties of zeolite-based multicomponent catalyst by combined gravimetric analysis and IR spectroscopy (AGIR), ACS Catal. 10 (12) (2020) 6822–6830.
[31] M. Schaefer, A. Thess, Modeling and simulation of closed low-pressure zeolite adsorbers for thermal energy storage, Int. J. Heat Mass Transfer 139 (2019) 685–699.
[32] J. Thomas, R. Tellgren, I. Olovsson, Hydrogen Bond Studies. Xcii. Disorder in (HCO3)22- and (DCO3)2-2 Dimers: a Neutron Diffraction Study of KHCO3 and KDCO3, Tech. Rep., Umeaa Univ., Sweden, 1974.
[33] C. Zhao, X. Chen, C. Zhao, Effect of crystal structure on CO2 capture characteristics of dry potassium-based sorbents, Chemosphere 75 (10) (2009) 1401–1404.
[34] M. Hartman, K. Svoboda, B. Čech, M. Pohořelý, M. Šyc, Decomposition of potassium hydrogen carbonate: thermochemistry, kinetics, and textural changes in solids, Ind. Eng. Chem. Res. 58 (8) (2019) 2868–2881.
[35] K.S. Sing, Reporting physisorption data for gas/solid systems with special reference to the determination of surface area and porosity (Recommendations 1984), Pure Appl. Chem. 57 (4) (1985) 603–619.
[36] H. Mittal, A. Al Alili, S.M. Alhassan, Adsorption isotherm and kinetics of water vapors on novel superporous hydrogel composites, Microporous Mesop. Mater. 299 (2020) 110106.
[37] C. Dai, A. Zhang, M. Liu, J. Li, F. Song, C. Song, X. Guo, Facile one-step synthesis of hierarchical porous carbon monoliths as superior supports of Fe-based catalysts for CO 2 hydrogenation, RSC Adv. 6 (13) (2016) 10831–10836.
[38] S. Vyazovkin, A.K. Burnham, J.M. Criado, L.A. Pérez-Maqueda, C. Popescu, N. Sbirrazzuoli, ICTAC Kinetics Committee recommendations for performing kinetic computations on thermal analysis data, Thermochimica Acta 520 (1–2) (2011) 1–19.
[39] L.-C. Sögütoglu, F. Birkelbach, A. Werner, H. Fischer, H. Huinink, O. Adan, Hydration of salts as a two-step process: Water adsorption and hydrate formation, Thermochim. Acta 695 (2021) 178819.

[40] W. Wei, L. Yang, Y. Li, G. Lu, M. Brookes, Y. Huang, X. Fan, Experimental and simulation study of two-stage water adsorption in salt porous composites for advanced thermochemical heat storage, Chem. Eng. J. 482 (2024) 149096.
[41] J. Szekely, J.W. Evans, H.Y. Sohn, Reactions of porous solids, Gas-solid React. (1976) 108–175.
[42] Z.-Y. Deng, J. She, Y. Inagaki, J.-F. Yang, T. Ohji, Y. Tanaka, Reinforcement by crack-tip blunting in porous ceramics, J. Eur. Ceram. Soc. 24 (7) (2004) 2055–2059.
[43] J. Aarts, H. Fischer, O. Adan, H. Huinink, Impact of cycling on the performance of mm-sized salt hydrate particles, J. Energy Storage 76 (2024) 109806.
[44] N. Mazur, H. Huinink, H. Fischer, O. Adan, Impact of atmospheric CO2 on thermochemical heat storage capabilities of K2CO3, Energy Fuels 36 (23) (2022) 14464–14475.
[45] M. Gaeini, S. Shaik, C. Rindt, Characterization of potassium carbonate salt hydrate for thermochemical energy storage in buildings, Energy Build. 196 (2019) 178–193.
[46] Q. Zhao, J. Lin, H. Huang, Z. Xie, Y. Xiao, Enhancement of heat and mass transfer of potassium carbonate-based thermochemical materials for thermal energy storage, J. Energy Storage 50 (2022) 104259.